

A Spectral Element Discontinuous Galerkin Thermal lattice Boltzmann method for Conjugate Heat Transfer applications

Saumil S. Patel^a, Misun Min^b, Kalu Chibueze Uga^a, Taehun Lee^{a,*}

^a*Department of Mechanical Engineering, City College of City University of New York,
New York, NY 10031, USA*

^b*Mathematics and Computer Science Division, Argonne National Laboratory, Argonne,
IL 60439, USA*

Abstract

We present a spectral-element discontinuous Galerkin thermal lattice Boltzmann method (SEDG-TLBM) for fluid-solid conjugate heat transfer applications. In this work, we revisit the discrete Boltzmann equation (DBE) for nearly incompressible flows and propose a numerical scheme for conjugate heat transfer applications on unstructured, non-uniform mesh distributions. We employ a double-distribution function thermal lattice Boltzmann model to resolve flows with variable Prandtl (Pr) number. Based upon its finite element “heritage”, the SEDG discretization provides an effective means to model and investigate thermal transport in applications with complex geometries. In particular, we numerically investigate the effect of Reynolds (Re) number on the conjugate heat transfer around a circular cylinder with

*Corresponding Author

Email addresses: saumil.patel1134@gmail.com (Saumil S. Patel),
mmin@mcs.anl.gov (Misun Min), uga.kalu@gmail.com (Kalu Chibueze Uga),
thlee@ccny.cuny.edu (Taehun Lee)

volumetric heat source. Our solutions are represented by the tensor product basis of the one-dimensional Legendre-Lagrange interpolation polynomials. A high-order discretization is employed on body-conforming hexahedral elements with Gauss-Lobatto-Legendre (GLL) quadrature nodes. Thermal and hydrodynamic bounce-back boundary conditions are imposed via the numerical flux formulation which arises due to the discontinuous Galerkin approach. As a result, our scheme does not require tedious extrapolation at the boundaries which may cause loss of mass conservation. Steady-state results are presented for $Re = 5 - 40$. In each case, we discuss the effect of Re on the heat flux (i.e. Nusselt number Nu) at the cylinder surface (i.e. fluid-solid interface). In addition, the influence of the Re number on the variation of the temperature distribution *within* the cylinder is studied. Our results are validated against the Navier-Stokes spectral-element based computational fluid dynamics (CFD) solver known as Nek5000.

Keywords: Conjugate Heat Transfer, Spectral-element method, Discontinuous Galerkin method, Lattice Boltzmann method

1. Introduction

Conjugate heat transfer (CHT) occurs when energy/heat is transferred between two different mediums that are in contact with each other. The process is observed in numerous engineering applications: the drying of different materials (paper, steel, glass), food processing, cooling of electronic circuits, and nuclear reactor processes. These examples generally involve a fluid that

is convected over a solid surface. In the context of an incompressible fluid, the density is independent of temperature whereby the energy conservation equation is decoupled from the momentum and mass conservation equations. In the absence of viscous dissipation, the energy (or temperature) is treated as a passive scalar and is governed by convective and diffusive processes (i.e. the advection-diffusion equation). Predicting the flow and temperature fields for CHT by means of computational fluid dynamic (CFD) solvers can be a difficult task, especially in complex geometries like a nuclear reactor core [1]. Another difficulty is to maintain the continuity of temperature and heat fluxes at the fluid-solid interface. While traditional CFD methods [2, 3] have proven successful in enforcing such boundary conditions, there is considerable computational cost associated with the implementation [4].

Incompressible flow past an isothermal circular cylinder and the associated convection heat transfer has been the subject of numerous research articles. This problem is of particular importance since it exhibits a rich and complicated flow structure around a relatively simply geometry. Yet, from a computational perspective, the geometry requires a careful arrangement of the mesh in order to capture the onset of the von Kármán vortex street. Jain and Goel [5], were one of the first to numerically investigate this problem using a finite-difference method. Later, using a spectral element method, Karniadakis [2] simulated forced convection heat transfer from a isolated cylinder in a cross-flow for Reynolds number $Re = 200$. A thorough review of the early numerical and experimental studies can be found in [3].

Many of these studies treat the cylinder with a prescribed constant temperature Dirichlet boundary condition, revealing no analysis on the conjugate heat transfer between the flow and interior of the cylinder. Understanding how the flow affects the temperature distribution *within* the cylinder has been the subject of some recent studies. Juncu [6] reported cylinder temperatures for $Re = 2$ and $Re = 20$. Das and Reddy [7] investigated natural convection flow in a square enclosure with a central solid conducting body where they use a finite-volume scheme to discretize the energy equations within the flow and solid regions. Jeon et al. [8] investigated both natural and forced convection heat transfer using the steady-state conservation equations where the solid conducting body now had a volumetric heat source.

The lattice Boltzmann method (LBM) [9] has emerged as a reliable method for simulating thermal flows and a thorough review of the relevant work can be found in [10]. There are a few studies that have investigated fluid-solid CHT via the lattice Boltzmann method. Wang et al. [4] proposed a double-distribution model which insured temperature and heat flux continuity at the fluid-solid interface. Yet, the scope of their applications were limited to simple Cartesian box geometries. Jami et al. [11] investigated natural convection with a heat-generating cylinder conducting body using a multiple-relaxation-time (MRT) lattice Boltzmann method to capture the flow field while using a macroscopic energy equation to resolve the temperature field. Yan and Zu [12] investigated flow past a rotating isothermal circular cylinder. Their work also incorporated a double-distribution model with a regular lattice grid

which requires a complex treatment to impose the hydrodynamic boundary conditions on a curved cylinder surface. In addition, thermal boundary conditions were realized through an extrapolation method which can sometimes lead to errors in conservation laws [13]. While these studies have been able to provide accurate and reasonable results, severe limitations persist when using regular Cartesian grids to capture the flow physics around curved or irregular boundaries. Considerable efforts for solving the discrete Boltzmann equation (DBE) on irregular grids have been published and we refer the reader to [13] to learn more.

The aim of this work is to propose a thermal lattice Boltzmann method (TLBM) for CHT problems which can capture heat transfer between a fluid and solid, along with the ensuing convection and/or diffusion of energy (temperature) within each medium, for relatively complex geometries with irregular mesh distributions. We adopt a double-distribution model [14, 15], where the discrete Boltzmann equation (DBE) for the density distribution function is solved to determine the momentum field and a thermal discrete Boltzmann equation (TDBE) for the internal energy distribution function is solved to determine the passive temperature field. Both equations are solved via a splitting scheme that is composed of a collision and streaming (linear advection) step. Our numerical scheme is based on the work of Min and Lee [13] who discretized the streaming step of the solution procedure using a spectral-element discontinuous Galerkin (SEDG) method. The approach benefits from a high-order spectral discretization which is based on the tensor

product basis given by the one-dimensional Legendre-Lagrange interpolation polynomials. As a result of choosing the SEDG discretization, we benefit from incorporating body-conforming hexahedral elements to mesh the computational domain and lay the groundwork to tackle future problems with more complex geometries. An additional advantage is the simple application of the bounce-back boundary condition through the numerical flux (an artifact of the discontinuous Galerkin approach). We can apply the bounce-back condition in an effort-less manner which does not call for further extrapolation or interpolation techniques as is done when using a regular Cartesian lattice for complex geometries. The continuity of temperature and heat flux across the fluid-solid interface is easily enforced by treating the temperature field in the entire computational domain as a continuous field. Abrupt changes in thermal diffusivity across the fluid-solid interface are properly reflected in the relaxation terms of the collision step. Numerical results on the forced convection of flow past a cylinder with a heat source are presented with this model. As a first step, we present steady-state results for $Re = 5 - 40$ and compare the SEDG-TLBM results to those provided by Nek5000 [16], an open-source Navier-Stokes solver based on the spectral-element method.

The paper is organized as follows. In Section 2, we present the governing equations, namely, the LBE for the mass and momentum fields and the thermal LBE for the temperature fields. In Section 3, we discuss the formulation of our numerical scheme. Section 4 presents computational results and their validation for forced convection past a circular cylinder with heat source.

We discuss our conclusions in Section 5. Details on the thermal boundary conditions are given in the Appendix.

2. Governing Equations

In this section, we describe the governing equations for conjugate heat transfer between nearly incompressible fluids and the hot solids with which the fluids are in perfect contact. First, we derive the lattice Boltzmann equation (LBE) for a nearly incompressible fluid. This equation is based solely on the density distribution function to obtain the mass and momentum fields. Next, following the model proposed by He et al. [15], we then present the evolution equation for the internal energy. Our formulation is a passive scalar approach and uses the additional evolution equations for internal energy to describe temperature.

2.1. Discrete Boltzmann Equation (DBE) for nearly incompressible fluids

The discrete Boltzmann equation with the Bhatnagar-Gross-Krook collision model [17] for nearly incompressible fluids is written in the following way:

$$\frac{\partial f_\alpha}{\partial t} + \mathbf{e}_\alpha \cdot \nabla f_\alpha = -\frac{f_\alpha - f_\alpha^{eq}}{\lambda_\nu} \quad (1)$$

where f_α ($\alpha = 0, 1, \dots, N_\alpha$) is the particle density distribution function defined in the direction of the microscopic velocity \mathbf{e}_α , λ_ν is the relaxation time, and N_α is the number of microscopic velocities. We consider the two-dimensional 9-velocity model (D2Q9) associated with $\mathbf{e}_\alpha = (0, 0)$ for

$\alpha = 0$; $\mathbf{e}_\alpha = (\cos \theta_\alpha, \sin \theta_\alpha)$ with $\theta_\alpha = (\alpha - 1)\pi/2$ for $\alpha = 1, 2, 3, 4$; and $\mathbf{e}_\alpha = \sqrt{2}(\cos \phi_\alpha, \sin \phi_\alpha)$ with $\phi_\alpha = (\alpha - 5)\pi/2 + \pi/4$ for $\alpha = 5, 6, 7, 8$.

The equilibrium distribution function is given by

$$f_\alpha^{eq} = t_\alpha \rho \left[1 + \frac{(\mathbf{e}_\alpha \cdot \mathbf{u})}{c_s^2} + \frac{(\mathbf{e}_\alpha \cdot \mathbf{u})^2}{2c_s^4} - \frac{(\mathbf{u} \cdot \mathbf{u})}{2c_s^2} \right], \quad (2)$$

where ρ is the density of the fluid; \mathbf{u} is the macroscopic velocity; $t_0 = 4/9$, $t_{\alpha=1,4} = 1/9$, and $t_{\alpha=5,8} = 1/36$ are the weights; and $c_s = 1/\sqrt{3}$ is the speed of sound [18].

2.2. Lattice Boltzmann Equation (LBE) for nearly incompressible fluids

The lattice Boltzmann equation is obtained by discretizing Eq. (1) over a time-step δt as shown in [10]

$$f_\alpha(\mathbf{x}, t) - f_\alpha(\mathbf{x} - \mathbf{e}_\alpha \delta t, t - \delta t) = - \int_{t-\delta t}^t \frac{f_\alpha - f_\alpha^{eq}}{\lambda_\nu} dt'. \quad (3)$$

We note that this temporal integration $[t - \delta t, t]$ is coupled with the space integration $[\mathbf{x} - \mathbf{e}_\alpha \delta t, \mathbf{x}]$. Applying the trapezoidal rule [19] for the integration on the right-hand side of Eq. (3), we have the following for each term

$$\int_{t-\delta t}^t \frac{f_\alpha - f_\alpha^{eq}}{\lambda_\nu} dt' \approx \frac{f_\alpha - f_\alpha^{eq}}{2\tau_\nu} \Big|_{(\mathbf{x} - \mathbf{e}_\alpha \delta t, t - \delta t)} + \frac{f_\alpha - f_\alpha^{eq}}{2\tau_\nu} \Big|_{(\mathbf{x}, t)} \quad (4)$$

and where the dimensionless relaxation time is $\tau_\nu = \lambda_\nu / \delta t$ with a relation to the kinematic viscosity by $\nu = \tau_\nu c_s^2 \delta t$.

Using Eq. (4), we can now write Eq. (3) as the lattice Boltzmann equation for a single-phase nearly incompressible fluid:

$$\bar{f}_\alpha(\mathbf{x}, t) = \bar{f}_\alpha(\mathbf{x} - \mathbf{e}_\alpha \delta t, t - \delta t) - \frac{1}{\tau + 1/2} (\bar{f}_\alpha - \bar{f}_\alpha^{eq})|_{(\mathbf{x} - \mathbf{e}_\alpha \delta t, t - \delta t)}. \quad (5)$$

Where \bar{f} and \bar{f}_α^{eq} are the modified particle and equilibrium distribution functions, respectively, and are defined as

$$\bar{f}_\alpha = f_\alpha + \frac{f_\alpha - f_\alpha^{eq}}{2\tau} \quad (6)$$

and

$$\bar{f}_\alpha^{eq} = f_\alpha^{eq} \quad (7)$$

Eq. (3) is then solved in two step:

- **Collision**

$$\bar{f}_\alpha^*(\mathbf{x}, t - \delta t) = \bar{f}_\alpha(\mathbf{x}, t - \delta t) - \frac{1}{\tau + 1/2} (\bar{f}_\alpha - \bar{f}_\alpha^{eq})|_{(\mathbf{x}, t - \delta t)} \quad (8)$$

which is followed by the substitution $\bar{f}_\alpha(\mathbf{x}, t - \delta t) = \bar{f}_\alpha^*(\mathbf{x}, t - \delta t)$.

- **Streaming**

$$\bar{f}_\alpha(\mathbf{x}, t) = \bar{f}_\alpha(\mathbf{x} - \mathbf{e}_\alpha \delta t, t - \delta t). \quad (9)$$

As it was shown in [10, 13] the streaming step of Eq. (9), can be expressed as a solution of the linear advection equation, written in an Eulerian frame-

work [20]:

$$\frac{\partial \bar{f}_\alpha}{\partial t} + \mathbf{e}_\alpha \cdot \nabla \bar{f}_\alpha = 0. \quad (10)$$

The density and momentum can be computed by taking moments as follows:

$$\rho = \sum_{\alpha=0}^{N_\alpha} \bar{f}_\alpha \quad \text{and} \quad \rho \mathbf{u} = \sum_{\alpha=0}^{N_\alpha} \mathbf{e}_\alpha \bar{f}_\alpha \quad (11)$$

The temperature, T , can be calculated from the density distribution function by taking the second moment of f_α . As it is noted in [15] and [21], the second moment yields a fixed Prandtl number which means that the thermal conductivity cannot be adjusted independent of the kinetic viscosity. Following the work of He et al. [15] and Guo et al. [22], we seek to investigate thermal flows with variable Prandtl number and choose not to use the density distribution function, f , to calculate the internal energy.

2.3. Discrete Boltzmann Equation (DBE) for internal energy

In this section, we describe the DBE for internal energy, e . We adopt the approach of He et al. [15] and introduce a new variable for internal energy density distribution function:

$$g_\alpha = \frac{(\mathbf{e}_\alpha - \mathbf{u})^2}{2} f_\alpha \quad (12)$$

Following the simplification of Peng et al. [23], where viscous heat dissipation and compression work by pressure are neglected, Eq. (12) now leads to the

following evolution equation for internal energy:

$$\frac{\partial g_\alpha}{\partial t} + \mathbf{e}_\alpha \cdot \nabla g_\alpha = -\frac{g_\alpha - g_\alpha^{eq}}{\lambda_e} + t_\alpha \dot{Q} \quad (13)$$

where λ_e is the relaxation time related to energy transport; t_α represents the non-dimensional weights described above and \dot{Q} is a constant volumetric heat generation term. As was done for the DBE in Eq. (1), we consider the two-dimensional 9-velocity model (D2Q9) mentioned above. The associated equilibrium distribution function, g_α^{eq} , is given as:

$$g_0^{eq} = -\frac{4\rho e}{9} \frac{(\mathbf{u} \cdot \mathbf{u})}{2c_s^2}, \quad (14)$$

$$g_{1,2,3,4}^{eq} = \frac{\rho e}{18} \left[\frac{1}{c_s^2} + \frac{(\mathbf{e}_\alpha \cdot \mathbf{u})}{c_s^2} + \frac{(\mathbf{e}_\alpha \cdot \mathbf{u}^2)}{c_s^4} - \frac{(\mathbf{u} \cdot \mathbf{u})}{c_s^2} \right], \quad (15)$$

$$g_{5,6,7,8}^{eq} = \frac{\rho e}{36} \left[\frac{1}{c_s^2} + \frac{2(\mathbf{e}_\alpha \cdot \mathbf{u})}{c_s^2} + \frac{(\mathbf{e}_\alpha \cdot \mathbf{u})^2}{2c_s^4} - \frac{(\mathbf{u} \cdot \mathbf{u})}{2c_s^2} \right], \quad (16)$$

2.4. Lattice Boltzmann Equation (LBE) for internal energy

The lattice Boltzmann equation for internal energy is now obtained in a manner similar to that of density distribution function, f_α . We begin by performing a coupled space-time integration over the timestep, δt , on Eq. (12):

$$g_\alpha(\mathbf{x}, t) - g_\alpha(\mathbf{x} - \mathbf{e}_\alpha \delta t, t - \delta t) = - \int_{t-\delta t}^t \frac{g_\alpha - g_\alpha^{eq}}{\lambda_e} dt' + \int_{t-\delta t}^t t_\alpha \dot{Q} dt'. \quad (17)$$

Using a trapezoidal rule for the integration of each term on the right hand side of Eq. (17) along with the follow variable substitutions:

$$\bar{g}_\alpha = g_\alpha + \frac{g_\alpha - g_\alpha^{eq}}{2\tau_e} - \frac{\delta t}{2} t_\alpha \dot{Q} \quad (18)$$

and

$$\bar{g}_\alpha^{eq} = g_\alpha^{eq} - \frac{\delta t}{2} t_\alpha \dot{Q} \quad (19)$$

Eq. (17) now becomes the following lattice Boltzmann equation for internal energy:

$$\begin{aligned} \bar{g}_\alpha(\mathbf{x}, t) &= \bar{g}_\alpha(\mathbf{x} - \mathbf{e}_\alpha \delta t, t - \delta t) - \frac{1}{\tau_e + 1/2} (\bar{g}_\alpha - \bar{g}_\alpha^{eq})|_{(\mathbf{x} - \mathbf{e}_\alpha \delta t, t - \delta t)} \\ &+ \delta t \dot{Q} t_\alpha, \end{aligned} \quad (20)$$

where the dimensionless relaxation time related to the internal energy is $\tau_e = \lambda_e / \delta t$ with a relation to the thermal diffusivity by $\chi = \frac{(D+2)\tau_e c_s^2 \delta t}{D}$. Eq. (20) is now solved via the following collision-streaming process:

- **Collision**

$$\begin{aligned} \bar{g}_\alpha^*(\mathbf{x}, t - \delta t) &= \bar{g}_\alpha(\mathbf{x}, t - \delta t) - \frac{1}{\tau_e + 1/2} (\bar{g}_\alpha - \bar{g}_\alpha^{eq})|_{(\mathbf{x}, t - \delta t)} \\ &+ t_\alpha \dot{Q} \delta t|_{(\mathbf{x}, t - \delta t)}, \end{aligned} \quad (21)$$

which is followed by the substitution $\bar{g}_\alpha(\mathbf{x}, t - \delta t) = \bar{g}_\alpha^*(\mathbf{x}, t - \delta t)$ and then the streaming process

- **Streaming**

$$\bar{g}_\alpha(\mathbf{x}, t) = \bar{g}_\alpha(\mathbf{x} - \mathbf{e}_\alpha \delta t, t - \delta t). \quad (22)$$

The streaming step of Eq. (22), can be expressed as a solution of the linear advection equation, written in an Eulerian framework [20]:

$$\frac{\partial \bar{g}_\alpha}{\partial t} + \mathbf{e}_\alpha \cdot \nabla \bar{g}_\alpha = 0. \quad (23)$$

The temperature, T , can be calculated by taking the moment:

$$\rho e = \sum_{\alpha=0}^{N_\alpha} \bar{g}_\alpha + \frac{\delta t}{2} \dot{Q} \quad (24)$$

where e is the internal energy and is related to the temperature by $e = DRT/2$ where D is the dimension and R is the gas constant.

3. Numerical Discretization

In this section, we present our computational scheme. We provide details to the discontinuous Galerkin strong formulation, numerical fluxes, and boundary conditions for Eqs. (10) and (23). Details on the spectral element discretizations and time-stepping schemes are also discussed.

3.1. Weak Formulation of LB Advection Equation

We formulate the weak form for Eqs. (10) and (23) defined on the computational domain $\Omega = \cup_{e=1}^E \Omega^e$ with non-overlapping elements Ω^e . We begin

by writing the global solutions, $\bar{f}_\alpha(\mathbf{x}, t)$ and $\bar{g}_\alpha(\mathbf{x}, t)$, which will be approximated by the piecewise N -th order polynomial approximations, $\bar{f}_\alpha(\mathbf{x}, t)_h$ and $\bar{g}_\alpha(\mathbf{x}, t)_h$,

$$\begin{aligned}\bar{f}_\alpha(\mathbf{x}, t) &\simeq \bar{f}_\alpha(\mathbf{x}, t)_h = \oplus_{e=1}^E \bar{f}_\alpha(\mathbf{x}, t)_h^e \\ \bar{g}_\alpha(\mathbf{x}, t) &\simeq \bar{g}_\alpha(\mathbf{x}, t)_h = \oplus_{e=1}^E \bar{g}_\alpha(\mathbf{x}, t)_h^e\end{aligned}\tag{25}$$

where the subscript h refers to a characteristic measure of the size of the element, Ω^e . $\bar{f}_\alpha(\mathbf{x}, t)_h^e$ and $\bar{g}_\alpha(\mathbf{x}, t)_h^e$ represents the local polynomial solution on the element Ω^e . The next step is to define a global space $V_{\alpha, h}$ of test functions, $\phi_{\alpha, h}$, such that $V_{\alpha, h} = \oplus_{e=1}^E V_{\alpha, h}^e$. The locally defined spaces $V_{\alpha, h}^e$ are defined by $V_{\alpha, h}^e = \text{span}\{\phi_{\alpha, h}^n\}_{n=1}^{N_p}$. Another way to describe $V_{\alpha, h}^e$ is the set of all linear combinations of $\phi_{\alpha, h}^n$ where N_p is the number of quadrature points that are defined on the element Ω^e . Details on the functional form of the test functions, $\phi_{\alpha, h}^n$, are given later in this paper. For now, we indicate that our locally defined solutions $\bar{f}_\alpha(\mathbf{x}, t)_h^e$ and $\bar{g}_\alpha(\mathbf{x}, t)_h^e$ are polynomials which are written as an expansion of the test functions:

$$\begin{aligned}\bar{f}_\alpha(\mathbf{x}, t)_h^e &= \sum_i^{N_p} (\bar{f}_\alpha^i(t)) \phi_{\alpha, h}^i(\mathbf{x}) \\ \bar{g}_\alpha(\mathbf{x}, t)_h^e &= \sum_i^{N_p} (\bar{g}_\alpha^i(t)) \phi_{\alpha, h}^i(\mathbf{x})\end{aligned}\tag{26}$$

With properly defined test functions $\phi_{\alpha, h}$, we multiply them with Eqs. (10) and (23), and integrate by parts twice in a manner similar to [13], where we

then obtain the following weak formulations:

$$\left(\frac{\partial \bar{f}_\alpha}{\partial t} + \nabla \cdot \mathbf{F}_\alpha(\bar{f}), \phi_{\alpha,h} \right)_{\Omega^e} = (\mathbf{n} \cdot [\mathbf{F}_\alpha(\bar{f}) - \mathbf{F}_\alpha^*(\bar{f})], \phi_{\alpha,h})_{\partial\Omega^e} \quad (27)$$

$$\left(\frac{\partial \bar{g}_\alpha}{\partial t} + \nabla \cdot \mathbf{G}_\alpha(\bar{g}), \phi_{\alpha,h} \right)_{\Omega^e} = (\mathbf{n} \cdot [\mathbf{G}_\alpha(\bar{g}) - \mathbf{G}_\alpha^*(\bar{g})], \phi_{\alpha,h})_{\partial\Omega^e} \quad (28)$$

where $\mathbf{F}_\alpha(\bar{f}) = \mathbf{e}_\alpha \bar{f}_\alpha$ and $\mathbf{G}_\alpha(\bar{g}) = \mathbf{e}_\alpha \bar{g}_\alpha$ represent the flux vectors for the density distribution function and internal energy distribution function, respectively. $\mathbf{e}_\alpha = (e_{\alpha x}, e_{\alpha y})$ are the microscopic velocities and $\mathbf{n} = (n_x, n_y)$ is the unit normal vector pointing outward on the element boundary, $\partial\Omega^e$. The numerical fluxes $\mathbf{F}_\alpha^*(\bar{f}) = \mathbf{F}_\alpha^*(\bar{f}, \bar{f}^+)$ and $\mathbf{G}_\alpha^*(\bar{g}) = \mathbf{G}_\alpha^*(\bar{g}, \bar{g}^+)$ in Eqs. (27) and (28) are a function of the local solution (i.e. $\bar{f}_\alpha, \bar{g}_\alpha$) and the neighboring solution (i.e. $\bar{f}_\alpha^+, \bar{g}_\alpha^+$) at the interfaces between neighboring elements. We choose the Lax-Friedrichs flux in [13, 24] which gives the following form for the integrand in the surface integrals of Eqs. (27) and (28):

$$\begin{aligned} \mathbf{n} \cdot (\mathbf{F}_\alpha - \mathbf{F}_\alpha^*) &= \begin{cases} (\mathbf{n} \cdot \mathbf{e}_\alpha)[\bar{f}_\alpha - \bar{f}_\alpha^+] & \text{for } \mathbf{n} \cdot \mathbf{e}_\alpha < 0, \\ 0 & \text{for } \mathbf{n} \cdot \mathbf{e}_\alpha \geq 0. \end{cases} \\ \mathbf{n} \cdot (\mathbf{G}_\alpha - \mathbf{G}_\alpha^*) &= \begin{cases} (\mathbf{n} \cdot \mathbf{e}_\alpha)[\bar{g}_\alpha - \bar{g}_\alpha^+] & \text{for } \mathbf{n} \cdot \mathbf{e}_\alpha < 0, \\ 0 & \text{for } \mathbf{n} \cdot \mathbf{e}_\alpha \geq 0. \end{cases} \end{aligned} \quad (29)$$

When $\mathbf{n} \cdot \mathbf{e}_\alpha < 0$, we can write

$$\begin{aligned}\mathbf{n} \cdot (\mathbf{F}_\alpha - \mathbf{F}_\alpha^*) &= (n_x e_{\alpha x} + n_y e_{\alpha y}) \bar{f}_\alpha + (n_x^+ e_{\alpha x} + n_y^+ e_{\alpha y}) \bar{f}_\alpha^+ \\ \mathbf{n} \cdot (\mathbf{G}_\alpha - \mathbf{G}_\alpha^*) &= (n_x e_{\alpha x} + n_y e_{\alpha y}) \bar{g}_\alpha + (n_x^+ e_{\alpha x} + n_y^+ e_{\alpha y}) \bar{g}_\alpha^+.\end{aligned}\quad (30)$$

The proper upwinding scheme, inherent in the Lax-Friedrichs flux, allows momentum transfer at the element interface to depend only on those particles that are entering into the element.

3.2. Boundary Conditions

Boundary conditions are weakly imposed through the numerical flux. The hydrodynamic wall boundary condition, with specific details provided in [13, 25], is given as follows:

$$\bar{f}_\alpha - \bar{f}_\alpha^+ = \begin{cases} \bar{f}_\alpha - \bar{f}_{\alpha^*} - 2t_\alpha \rho_0 (\mathbf{e}_\alpha \cdot \mathbf{u}_b) / c_s^2 & \text{for } \mathbf{n} \cdot \mathbf{e}_\alpha < 0 \\ 0 & \text{for } \mathbf{n} \cdot \mathbf{e}_\alpha \geq 0, \end{cases} \quad (31)$$

where \bar{f}_{α^*} is the particle distribution function moving in the opposite direction of \bar{f}_α , \mathbf{u}_b is the macroscopic velocity prescribed at the wall boundary, and ρ_0 is the reference density, chosen to be unity.

Constant Dirichlet thermodynamic boundary conditions are based on the bounce-back rule for the non-equilibrium internal energy distribution [15]:

$$\bar{g}_\alpha^{neq} - \mathbf{e}_\alpha^2 \bar{f}_\alpha^{neq,iso} = -(\bar{g}_{\alpha^*}^{neq} - \mathbf{e}_{\alpha^*}^2 \bar{f}_{\alpha^*}^{neq,iso}). \quad (32)$$

where \mathbf{e}_α and \mathbf{e}_{α^*} have opposite directions. As was mentioned in [15], $\bar{f}_\alpha^{neq,iso}$ is the non equilibrium density distribution function which neglects any heat flux contributions and is solely used to treat isothermal (*iso*) boundaries. The following relations for non-equilibrium are used: $\bar{f}_\alpha^{neq} = \bar{f}_\alpha - \bar{f}_\alpha^{eq}$ and $\bar{g}_\alpha^{neq} = \bar{g}_\alpha - \bar{g}_\alpha^{eq}$. Using these relations, an expression for \bar{g}_α^+ in Eq. (29) can be determined (see Appendix for further details). We arrive at the following formulation for the discontinuous Galerkin thermal boundary condition:

In the case of $\alpha = 1, 2, 3, 4$. Then,

$$\bar{g}_\alpha - \bar{g}_\alpha^+ = \begin{cases} \Theta_{\alpha,1-4} & \text{for } \mathbf{n} \cdot \mathbf{e}_\alpha < 0 \\ 0 & \text{for } \mathbf{n} \cdot \mathbf{e}_\alpha \geq 0 \end{cases} \quad (33)$$

and for $\alpha = 5, 6, 7, 8$:

$$\bar{g}_\alpha - \bar{g}_\alpha^+ = \begin{cases} \Theta_{\alpha,5-8} & \text{for } \mathbf{n} \cdot \mathbf{e}_\alpha < 0 \\ 0 & \text{for } \mathbf{n} \cdot \mathbf{e}_\alpha \geq 0 \end{cases} \quad (34)$$

where

$$\begin{aligned} \Theta_{\alpha,1-4} = & \bar{g}_\alpha + \bar{g}_{\alpha^*} - \frac{2\rho e_b}{9} [3 + 4.5(\mathbf{e}_\alpha \cdot \mathbf{u}_b)^2 - 1.5(\mathbf{u}_b \cdot \mathbf{u}_b)] + t_\alpha \dot{Q} \delta t \\ & - \mathbf{e}_\alpha^2 (\bar{f}_\alpha + \bar{f}_{\alpha^*}) + \mathbf{e}_\alpha^2 (2t_\alpha \rho [1 + 4.5(\mathbf{e}_\alpha \cdot \mathbf{u}_b)^2 - 1.5(\mathbf{u}_b \cdot \mathbf{u}_b)]) . \end{aligned}$$

$$\begin{aligned} \Theta_{\alpha,5-8} = & \bar{g}_\alpha + \bar{g}_{\alpha^*} - \frac{2\rho e_b}{36} [3 + 4.5(\mathbf{e}_\alpha \cdot \mathbf{u}_b)^2 - 1.5(\mathbf{u}_b \cdot \mathbf{u}_b)] + t_\alpha \dot{Q} \delta t \\ & - \mathbf{e}_\alpha^2 (\bar{f}_\alpha + \bar{f}_{\alpha^*}) + \mathbf{e}_\alpha^2 (2t_\alpha \rho [1 + 4.5(\mathbf{e}_\alpha \cdot \mathbf{u}_b)^2 - 1.5(\mathbf{u}_b \cdot \mathbf{u}_b)]) . \end{aligned}$$

Since this is the thermal boundary condition we note e_b is the prescribed internal energy at the boundary which simply translates to a Dirichlet temperature boundary condition. Further details on the boundary conditions can be found in the Appendix.

3.3. Spectral element discretizations

In this section we describe the functional form of the test function $\phi_{\alpha,h}$. These functions are actually chosen from the space of one-dimensional Legendre-Lagrange interpolation polynomials which are formally given as [26]:

$$l_i(\xi) = N(N+1)^{-1}(1-\xi^2)L'_N(\xi)/(\xi-\xi_i)L_N(\xi_i) \quad \text{for } \xi \in [-1, 1], \quad (35)$$

where ξ_i are the Gauss-Lobatto-Legendre (GLL) quadrature nodes and $L_N(\xi)$ is the N th-order Legendre polynomial. Our choice to use quadrilateral elements, Ω^e , to fill our two-dimensional computational domain, $\Omega = \cup_{e=1}^E \Omega^e$, enables us to benefit from the tensor-product basis which is created with Eq. (35). Each coordinate $(x, y) \in \Omega^e$ is mapped on the reference domain, $(\xi, \eta) \in I := [-1, 1]^2$, through the Gordon-Hall mapping [26]. The tensor-product structure of the reference element I allows us to define a two-dimensional basis, $\psi_{ij}(\xi, \eta) = l_i(\xi(x))l_j(\eta(y)) = \phi$. The equality to ϕ is used to make the functional form of the test functions clear to the reader. We

now replace the test functions used in Eqs. (26) with ψ_{ij} and write:

$$\bar{f}_\alpha^N(\mathbf{x}, t)_h^e = \sum_{i,j=0}^N (\bar{f}_\alpha^N)_{ij} \psi_{ij} \quad \text{and} \quad \bar{g}_\alpha^N(\mathbf{x}, t)_h^e = \sum_{i,j=0}^N (\bar{g}_\alpha^N)_{ij} \psi_{ij} \quad (36)$$

which are the local approximate solutions \bar{f}_α^N and \bar{g}_α^N written as the finite expansion of the ψ_{ij} on Ω^e . $(f_\alpha^N)_{ij} = f_\alpha^N(x_i, y_j, t)$ and $(\bar{g}_\alpha^N)_{ij} = g_\alpha^N(x_i, y_j, t)$ represents the approximate solution \bar{f}_α^N and \bar{g}_α^N on the nodal points (x_i, y_j) at time t . Plugging the approximate solutions of Eqs. (36) into their respective weak formulations (i.e. Eqs. (27) and (28)) we will then arrive the following semi-discrete scheme:

$$\frac{d\bar{\mathbf{f}}_\alpha}{dt} + \mathbf{M}^{-1} \mathbf{D} \bar{\mathbf{f}}_\alpha = \mathbf{M}^{-1} \mathbf{R}_f \bar{\mathbf{f}}_\alpha, \quad (37)$$

$$\frac{d\bar{\mathbf{g}}_\alpha}{dt} + \mathbf{M}^{-1} \mathbf{D} \bar{\mathbf{g}}_\alpha = \mathbf{M}^{-1} \mathbf{R}_g \bar{\mathbf{g}}_\alpha, \quad (38)$$

where the solution vectors are defined by $\bar{\mathbf{f}}_\alpha = [(\bar{f}_\alpha^N)_{ij}]$, and $\bar{\mathbf{g}}_\alpha = [(\bar{g}_\alpha^N)_{ij}]$ on a local element. The mass matrix is defined as

$$\mathbf{M} = (\psi_{ij}, \psi_{ij})_{\Omega^e} = J(\hat{M} \otimes \hat{M}), \quad (39)$$

where $\hat{M}_{ii} = \sum_{k=0}^N l_i(\xi_k) l_i(\xi_k) w_k$ is the one-dimensional mass matrix with the quadrature weight w_k defined on the reference domain $[-1, 1]$ and $J = [J_{ll}] = \text{diag}\{J_{ij}\}$ represents the value of the Jacobian at each node (x_i, y_j) with $l = i + (N+1)j$ on Ω^e . The one-dimensional mass matrix \hat{M} is diagonal

because of the orthogonal property of the Legendre-Lagrange interpolation polynomials on the GLL nodes, and thus the two-dimensional mass matrix \mathbf{M} is also diagonal. The gradient matrices are defined by

$$\mathbf{D} = e_{\alpha x} \mathbf{D}_x + e_{\alpha y} \mathbf{D}_y, \quad (40)$$

where the differentiation matrices can be represented by a tensor product form of the one-dimensional differentiation matrix $\hat{D} = [\hat{D}_{ii}] = l'_i(\xi_i)$ as

$$\mathbf{D}_x = \left(\frac{\partial \psi_{ij}}{\partial x}, \psi_{i\hat{j}} \right) = G^{\xi x} J[\hat{M} \otimes \hat{M} \hat{D}] + G^{\eta x} J[\hat{M} \hat{D} \otimes \hat{M}], \quad (41)$$

$$\mathbf{D}_y = \left(\frac{\partial \psi_{ij}}{\partial y}, \psi_{i\hat{j}} \right) = G^{\xi y} J[\hat{M} \otimes \hat{M} \hat{D}] + G^{\eta y} J[\hat{M} \hat{D} \otimes \hat{M}], \quad (42)$$

where $G^{\xi x}$, $G^{\xi y}$, $G^{\eta x}$, and $G^{\eta y}$ represent diagonal matrices for the geometric factors $\frac{\partial \xi}{\partial x}$, $\frac{\partial \xi}{\partial y}$, $\frac{\partial \eta}{\partial x}$, and $\frac{\partial \eta}{\partial y}$, respectively, at the nodal points (x_i, y_j) . The surface integrations acting on the boundary nodes on each face of the local element in Eqs. (37)–(38) are represented by

$$\mathbf{R}_f \bar{\mathbf{f}}_\alpha = \sum_{s=1}^4 \sum_{k=0}^N \mathcal{R}_k^s \{ \mathbf{n} \cdot [\mathbf{F}_\alpha(\bar{f}) - \mathbf{F}_\alpha^*(\bar{f})] \} w_k J_k^s, \quad (43)$$

$$\mathbf{R}_g \bar{\mathbf{g}}_\alpha = \sum_{s=1}^4 \sum_{k=0}^N \mathcal{R}_k^s \{ \mathbf{n} \cdot [\mathbf{G}_\alpha(\bar{g}) - \mathbf{G}_\alpha^*(\bar{g})] \} w_k J_k^s, \quad (44)$$

where $R_k^s\{\cdot\}$ extracts the information of $\{\cdot\}$ at the nodes situated on each face of the local element for the face number s and J_k^s is the surface Jacobian at the nodes on each face.

4. Numerical Results

In this section, we show computational results and validation for conjugate heat transfer of flow past a heated solid cylinder. We begin with a brief discussion of how relevant parameters are determined.

4.1. Parameters for Numerical Studies

We characterize forced convection flows with three nondimensional numbers, the Reynolds number (Re), Prandtl number (Pr), and thermal diffusivity ratio (γ) between the solid cylinder and fluid. They are defined as follows:

$$Re = \frac{U_i D}{\nu_f}, \quad Pr = \frac{\nu_f}{\chi_f}, \quad \text{and} \quad \gamma = \frac{\chi_s}{\chi_f}, \quad (45)$$

where U_i is the inflow boundary velocity in our simulation, D is the diameter of the cylinder, ν_f is the kinematic viscosity, and χ_f is the thermal diffusivity of the fluid. Ma is the Mach number in our simulation and is chosen to be $Ma \approx 0.01$. Our choice for Re will vary from $Re = 5 - 40$, while we will keep fluid and solid properties (i.e. ν_f , χ_f , and χ_s) fixed and hence fix Pr and γ . Our aim is to simulate a situation where water is flowing past a heat generating solid carbon steel cylinder. At 25° Celsius, this means $Pr \approx 6$ and $\gamma \approx 90$.

In order to validate our results, the heat source term \dot{Q} is non-dimensionalized via the diffusive time scale $t \sim D^2/\chi_f$. We write the non-dimensionalized

heat source term via:

$$\dot{Q}^* = \frac{\dot{Q}D^2}{\chi_f T_i \rho c_p} \quad (46)$$

with T_i being some characteristic temperature in the computational domain.

4.2. Flow past a heated cylinder

The schematic description to this problem is shown in Figure 1. At time, $t^* = 0$, there is a potential flow with the temperature in the entire computational domain to be T_i . Where t^* represents the nondimensional time $t^* = \frac{2U_i t}{D}$. The flow entering the domain is prescribed with a temperature T_i and velocity $\mathbf{u}_b = (U_i, 0)$. Figures 2 and 3 show the mesh which our computations are performed upon. The cylindrical surface is represented by a thicker black line as can be seen in Figure 3. We mesh within the cylinder and immediately downstream of the cylinder with additional refinement in order to capture the symmetric vortex structure that is created. The polynomials interpolation we employ is of order $N = 5$. Figure 4 shows the initial flow pattern that we employed for the simulation which is a potential flow. This automatically introduces a slip velocity on the surface of the cylinder with a vortex sheet of zero thickness. At $t > 0$ we impose $\mathbf{u}_b = (0, 0)$ on the surface of the cylinder. Figure 5 shows steady-state streamlines and isotherms for $Re = 5 - 40$. We observe how the isotherm profile changes and is advected as the flow matures to it's steady-state. We also see how the hotter isotherms remain near to the heated cylinder while the cooler isotherms are advected

and elongated further downstream of the cylinder. Upon further investigation it seems as though the isotherms are cooling down as the Reynolds number increases. Figure 6 shows the steady-state surface temperature distribution along the cylinder surface. Degrees are measured starting from 0 at the front (left) of the cylinder center and rotating counter-clockwise to 180, at the rear of the cylinder. We compare the SEDG-TLBM results against the Nek5000 results for the same polynomial order, $N = 5$. In each case, the average temperature difference between the two profiles is about a 0.3% error so we believe the results agree well. We also plot the maximum temperature within the cylinder in Figure 7 which provides evidence to confirm that the temperature within the cylinder decreases as the Re increases. Since there is circular symmetry in our problem the maximum temperature is located along the horizontal diameter of the circle. It's worthwhile to note that the maximum temperature location moves further away from the center and back towards the rear of the cylinder as Re changes from 5 to 20. Between $Re = 20 - 40$ we see that this max. temperature location moves back toward the center. This is most likely due to the separation region where stronger reverse flow impinges upon the rear of the cylinder. Similar results were found in [8].

The steady-state local Nusselt number along the cylindrical surface is plotted in Figure 8. We define Nu^* via

$$Nu^* = -\frac{D}{T_i} \left(\frac{\partial T}{\partial \mathbf{n}} \right)_{cylinder}, \quad (47)$$

where \mathbf{n} represents the outward pointing normal on the cylinder surface. Towards the front of the cylinder we can observe that heat transfer increases with Re . This is due to the dominating convection effect which the fluid has over its own thermal diffusivity (i.e. Peclet number, $Pe = \frac{U_i D}{\chi_f} > 1$). As the fluid travels over the cylinder surface, the effect of the Reynolds number Re plays a noticeable difference in the heat transfer. In particular, the heat flux towards the rear of the cylinder for $Re = 5$ is greater over the higher cases. This is most likely due to the absence of the vortex structure arising from the separation. At lower Re , the temperature of the cylinder is higher (especially towards the rear of the cylinder - as can be seen in Figure 6) and there is less of a reverse flow, which allows for higher heat flux to dominate between a hot, heat-generating solid cylinder and the cooler fluid. As Re increases, the separation region increases thus trapping more fluid. At steady-state, the temperature in the cylinder decreases (again see Figure 6) and the greater volume of fluid in this separation region allows for thermal heat transfer whereby the temperature difference between the two mediums becomes smaller thus decreasing the local heat flux. We also notice that the heat flux at the most rear location (180°) for $Re = 40$ is higher than the other cases. This, again, is probably due to the separation where the flow which impinges upon the cylinder at 180° is dominating the heat transfer process. This effect can be seen by the compression of isotherms in Figure 5(c) for the $Re = 40$ case.

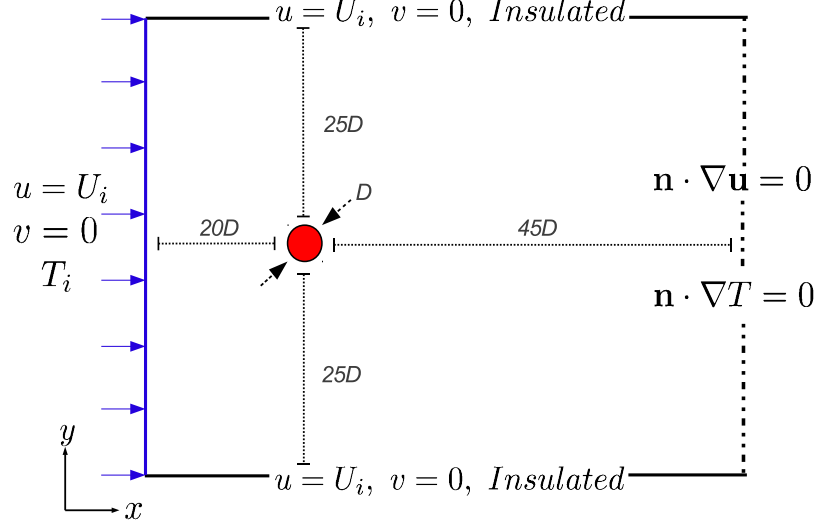


Figure 1: Schematic for the conjugate heat transfer of flow past a cylinder with heat source.

5. Conclusions

We have presented a spectral-element discontinuous Galerkin thermal lattice Boltzmann method (SEDG-TLBM) for solving fluid-solid conjugate heat transfer (CHT) problems. Our method provides accurate results for CHT applications in complex geometries and hence can incorporate lattice Boltzmann-based boundary conditions in a relatively straightforward manner. The technique comes at little cost in comparison to other LB algorithms which require extrapolation to approximate boundaries. Flow past a volumetrically heated solid cylinder is simulated using the SEDG-TLBM. As a first-step, steady-state calculations are performed to exhibit the capabilities of the algorithm. By treating the computational domain as one medium

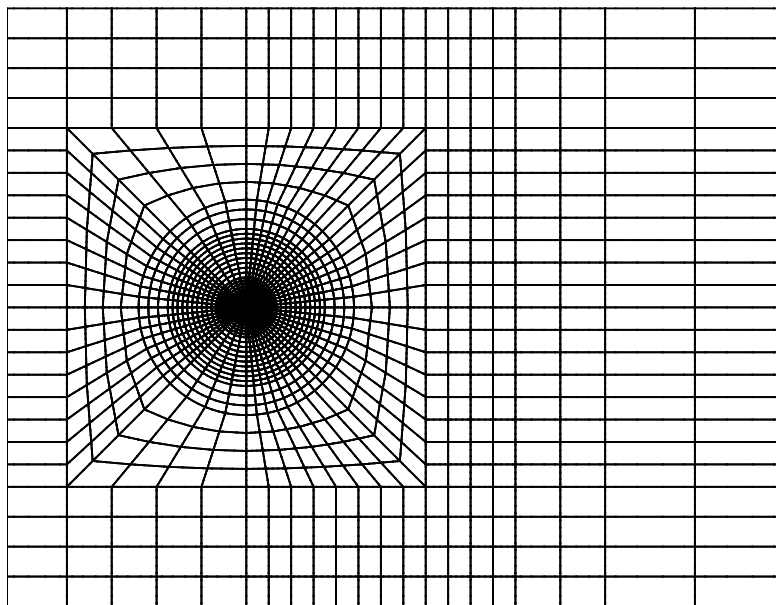


Figure 2: Mesh for the conjugate heat transfer of flow past a cylinder with heat source. Total number of elements is approx. 2,100. Polynomial order is $N = 5$.

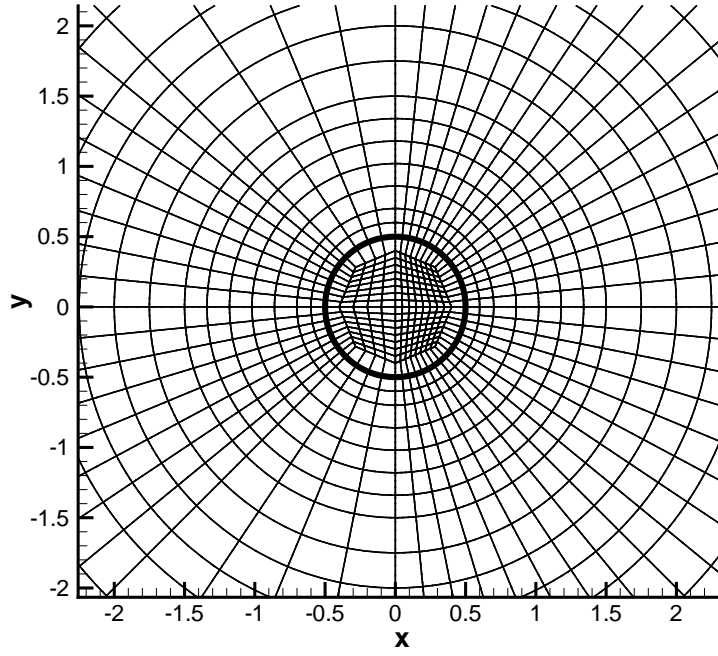


Figure 3: Mesh near the cylinder. Thicker black line represents the cylinder surface. Polynomial order is $N = 5$.

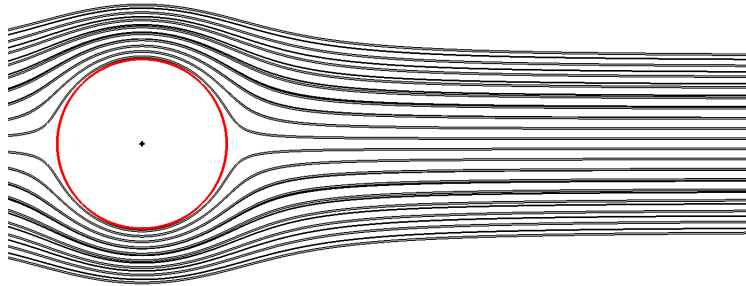
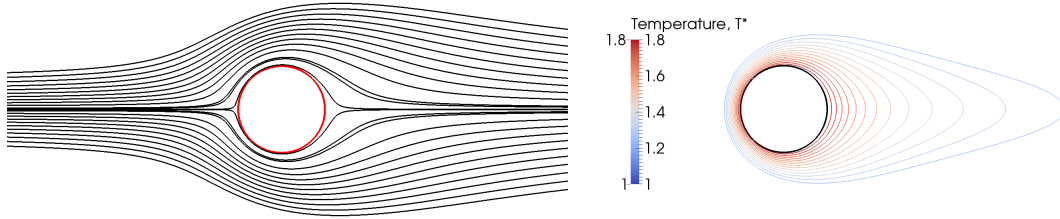
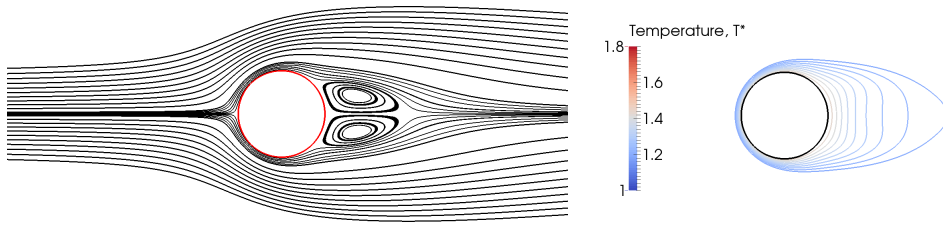


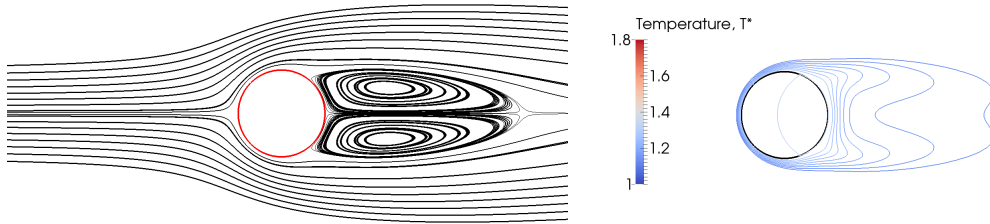
Figure 4: streamlines of potential flow which represent the initial flow conditions. $t^* = 0$.



(a) $Re = 5$



(b) $Re = 20$



(c) $Re = 40$

Figure 5: Steady State ($t^* = \infty$) streamlines(left) and isotherms(right) for forced convection past a cylinder with heat generating cylinder at $Re = 5, 20$, and 40

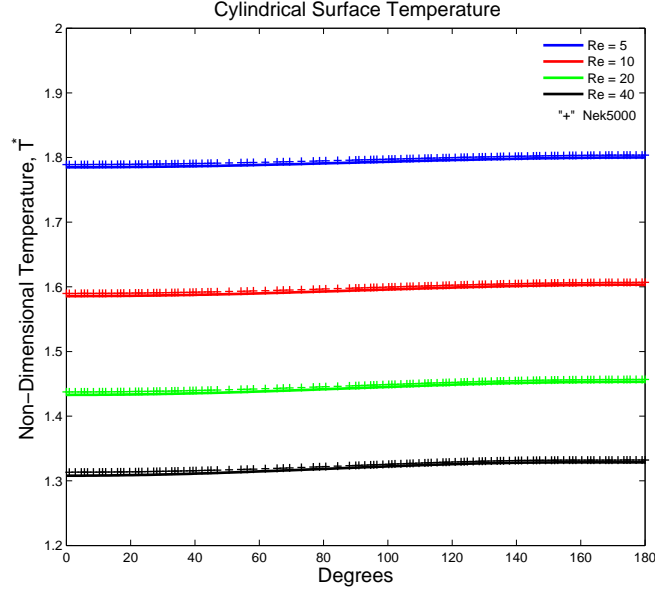


Figure 6: Steady-State non-dimensional temperature, $T^* = T/T_i$ along the upper half of cylindrical surface for $Re = 5 - 40$. The symbol (+) indicates the results from the Nek5000 Navier-Stokes solver.

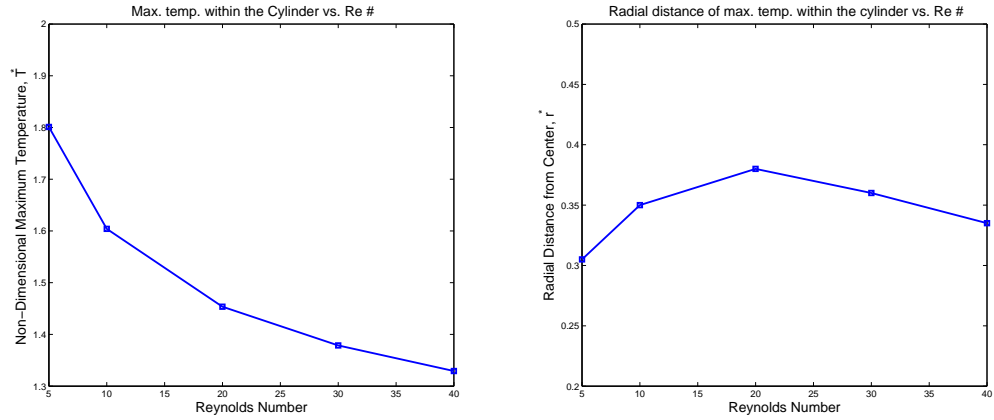


Figure 7: Maximum Temperatures and respective distance from center of cylinder for $Re = 5 - 40$.

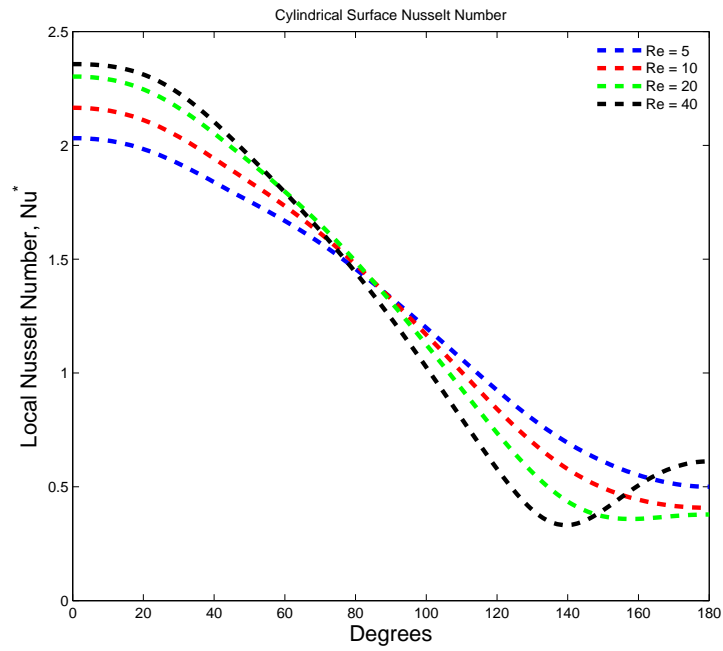


Figure 8: Steady-State Nusselt Numbers, Nu^* along upper half of cylindrical surface for $Re = 5 - 40$.

with discontinuous material properties (i.e. thermal diffusivity), temperature and heat flux continuity is ensured in our simulation with no additional work required. We examine the situation where water is flowing past a solid heat-conducting carbon cylinder for $Re = 5 - 40$. In each case, we observe a cooling of the cylinder as Re increases.

6. Appendix

In this appendix, we provide more details on the derivation of the thermal boundary conditions described in Eqs. (33) and (34). Using the relations, $\bar{f}_\alpha^{neq} = \bar{f}_\alpha - \bar{f}_\alpha^{eq}$ and $\bar{g}_\alpha^{neq} = \bar{g}_\alpha - \bar{g}_\alpha^{eq}$, we may write Eq. (32) as the following:

$$\bar{g}_\alpha - \bar{g}_\alpha^{eq} = -(\bar{g}_{\alpha^*} - \bar{g}_{\alpha^*}^{eq}) + \mathbf{e}_\alpha^2(\bar{f}_\alpha - \bar{f}_\alpha^{eq}) + \mathbf{e}_{\alpha^*}^2(\bar{f}_{\alpha^*} - \bar{f}_{\alpha^*}^{eq}), \quad (48)$$

noting that $\mathbf{e}_\alpha = -\mathbf{e}_{\alpha^*}$ and $\mathbf{e}_\alpha^2 = \mathbf{e}_{\alpha^*}^2$, Eq. (48) can be rearranged as

$$\bar{g}_\alpha = -\bar{g}_{\alpha^*} + (\bar{g}_\alpha^{eq} + \bar{g}_{\alpha^*}^{eq}) + \mathbf{e}_\alpha^2(\bar{f}_\alpha + \bar{f}_{\alpha^*}) - \mathbf{e}_\alpha^2(\bar{f}_\alpha^{eq} + \bar{f}_{\alpha^*}^{eq}) \quad (49)$$

For $\alpha = 1, 2, \dots, 8$;

$$\bar{f}_\alpha^{eq} + \bar{f}_{\alpha^*}^{eq} = 2t_\alpha \rho_0 [1 + 4.5(\mathbf{e}_\alpha \cdot \mathbf{u}_b)^2 - 1.5(\mathbf{u}_b \cdot \mathbf{u}_b)], \quad (50)$$

For $\alpha = 1, 2, 3, 4$;

$$\bar{g}_\alpha^{eq} + \bar{g}_{\alpha^*}^{eq} = \frac{2\rho_0 e_b}{9} [1.5 + 4.5(\mathbf{e}_\alpha \cdot \mathbf{u}_b)^2 - 1.5(\mathbf{u}_b \cdot \mathbf{u}_b)] - t_\alpha \dot{Q} \delta t, \quad (51)$$

For $\alpha = 5, 6, 7, 8$;

$$\bar{g}_\alpha^{eq} + \bar{g}_{\alpha^*}^{eq} = \frac{2\rho_0 e_b}{36} [3 + 4.5(\mathbf{e}_\alpha \cdot \mathbf{u}_b)^2 - 1.5(\mathbf{u}_b \cdot \mathbf{u}_b)] - t_\alpha \dot{Q} \delta t, \quad (52)$$

Substituting Eqns. (50), (51) and (52) into (49), we have:

For $\alpha = 1, 2, 3, 4$;

$$\begin{aligned}\bar{g}_\alpha &= -\bar{g}_{\alpha^*} + \frac{2\rho_0 e_b}{9} \left[1.5 + 4.5(\mathbf{e}_\alpha \cdot \mathbf{u}_b)^2 - 1.5(\mathbf{u}_b \cdot \mathbf{u}_b) \right] - t_\alpha \dot{Q} \delta t \\ &\quad + \mathbf{e}_\alpha^2 (\bar{f}_\alpha + \bar{f}_{\alpha^*}) - \mathbf{e}_\alpha^2 \left(2t_\alpha \rho_0 \left[1 + 4.5(\mathbf{e}_\alpha \cdot \mathbf{u}_b)^2 - 1.5(\mathbf{u}_b \cdot \mathbf{u}_b) \right] \right),\end{aligned}$$

For $\alpha = 5, 6, 7, 8$;

$$\begin{aligned}\bar{g}_\alpha &= -\bar{g}_{\alpha^*} + \frac{2\rho_0 e_b}{36} \left[3 + 4.5(\mathbf{e}_\alpha \cdot \mathbf{u}_b)^2 - 1.5(\mathbf{u}_b \cdot \mathbf{u}_b) \right] - t_\alpha \dot{Q} \delta t \\ &\quad + \mathbf{e}_\alpha^2 (\bar{f}_\alpha + \bar{f}_{\alpha^*}) - \mathbf{e}_\alpha^2 \left(2t_\alpha \rho_0 \left[1 + 4.5(\mathbf{e}_\alpha \cdot \mathbf{u}_b)^2 - 1.5(\mathbf{u}_b \cdot \mathbf{u}_b) \right] \right).\end{aligned}$$

Upon substitution of the expressions above into \bar{g}_α^+ , we arrive at the expressions given by Eqs. (33) and (34).

Below are specific formulations based on the microscopic directions α & α^* :

$$\begin{aligned}
\text{if } \mathbf{e}_1 \cdot \mathbf{n} < 0 \ (\Leftrightarrow \mathbf{e}_3 \cdot \mathbf{n} > 0); \quad \bar{g}_1 - \bar{g}_1^+ &= [\bar{g}_1 + \bar{g}_3] \\
&- \frac{2\rho_0 e_b}{9} [1.5 + 4.5(\mathbf{e}_1 \cdot \mathbf{u}_b)^2 - 1.5(\mathbf{u}_b \cdot \mathbf{u}_b)] \\
&+ t_1 \dot{Q} \delta t + \mathbf{e}_1^2 (\bar{f}_1 + \bar{f}_3) \\
&- \mathbf{e}_1^2 (2t_1 \rho [1 + 4.5(\mathbf{e}_1 \cdot \mathbf{u}_b)^2 - 1.5(\mathbf{u}_b \cdot \mathbf{u}_b)]) , \\
\bar{g}_3 - \bar{g}_3^+ &= [\bar{g}_3 - \bar{g}_1] = 0,
\end{aligned}$$

$$\begin{aligned}
\text{if } \mathbf{e}_2 \cdot \mathbf{n} < 0 \ (\Leftrightarrow \mathbf{e}_4 \cdot \mathbf{n} > 0); \quad \bar{g}_2 - \bar{g}_2^+ &= [\bar{g}_2 + \bar{g}_4] \\
&- \frac{2\rho e_b}{9} [1.5 + 4.5(\mathbf{e}_2 \cdot \mathbf{u})^2 - 1.5(\mathbf{u}_b \cdot \mathbf{u}_b)] \\
&+ t_2 \dot{Q} \delta t + \mathbf{e}_2^2 (\bar{f}_2 + \bar{f}_4) \\
&- \mathbf{e}_2^2 (2t_2 \rho [1 + 4.5(\mathbf{e}_2 \cdot \mathbf{u}_b)^2 - 1.5(\mathbf{u}_b \cdot \mathbf{u}_b)]) , \\
\bar{g}_4 - \bar{g}_4^+ &= [\bar{g}_4 - \bar{g}_2] = 0,
\end{aligned}$$

$$\begin{aligned}
\text{if } \mathbf{e}_3 \cdot \mathbf{n} < 0 \ (\Leftrightarrow \mathbf{e}_1 \cdot \mathbf{n} > 0); \quad \bar{g}_3 - \bar{g}_3^+ &= [\bar{g}_3 + \bar{g}_1] \\
&- \frac{2\rho e_b}{9} [1.5 + 4.5(\mathbf{e}_3 \cdot \mathbf{u}_b)^2 - 1.5(\mathbf{u}_b \cdot \mathbf{u}_b)] \\
&+ t_3 \dot{Q} \delta t + \mathbf{e}_3^2 (\bar{f}_3 + \bar{f}_1) \\
&- \mathbf{e}_3^2 (2t_3 \rho [1 + 4.5(\mathbf{e}_3 \cdot \mathbf{u}_b)^2 - 1.5(\mathbf{u}_b \cdot \mathbf{u}_b)]) , \\
\bar{g}_1 - \bar{g}_1^+ &= [\bar{g}_1 - \bar{g}_3] = 0,
\end{aligned}$$

$$\begin{aligned}
\text{if } \mathbf{e}_4 \cdot \mathbf{n} < 0 \quad (\Leftrightarrow \mathbf{e}_2 \cdot \mathbf{n} > 0); \quad \bar{g}_4 - \bar{g}_4^+ &= [\bar{g}_4 + \bar{g}_2] \\
&- \frac{2\rho e_b}{9} [1.5 + 4.5(\mathbf{e}_4 \cdot \mathbf{u}_b)^2 - 1.5(\mathbf{u}_b \cdot \mathbf{u}_b)] \\
&+ t_4 \dot{Q} \delta t + \mathbf{e}_2^2 (\bar{f}_2 + \bar{f}_4) \\
&- \mathbf{e}_4^2 (2t_4 \rho [1 + 4.5(\mathbf{e}_4 \cdot \mathbf{u}_b)^2 - 1.5(\mathbf{u}_b \cdot \mathbf{u}_b)]) , \\
\bar{g}_2 - \bar{g}_2^+ &= [\bar{g}_2 - \bar{g}_4] = 0,
\end{aligned}$$

$$\begin{aligned}
\text{if } \mathbf{e}_5 \cdot \mathbf{n} < 0 \quad (\Leftrightarrow \mathbf{e}_7 \cdot \mathbf{n} > 0); \quad \bar{g}_5 - \bar{g}_5^+ &= [\bar{g}_5 + \bar{g}_7] \\
&- \frac{2\rho e_b}{36} [3.0 + 4.5(\mathbf{e}_5 \cdot \mathbf{u}_b)^2 - 1.5(\mathbf{u}_b \cdot \mathbf{u}_b)] \\
&+ t_5 \dot{Q} \delta t + \mathbf{e}_2^2 (\bar{f}_5 + \bar{f}_7) \\
&- \mathbf{e}_5^2 (2t_5 \rho [1 + 4.5(\mathbf{e}_5 \cdot \mathbf{u}_b)^2 - 1.5(\mathbf{u}_b \cdot \mathbf{u}_b)]) , \\
\bar{g}_7 - \bar{g}_7^+ &= [\bar{g}_7 - \bar{g}_5] = 0,
\end{aligned}$$

$$\begin{aligned}
\text{if } \mathbf{e}_6 \cdot \mathbf{n} < 0 \quad (\Leftrightarrow \mathbf{e}_8 \cdot \mathbf{n} > 0); \quad \bar{g}_6 - \bar{g}_6^+ &= [\bar{g}_6 + \bar{g}_8] \\
&- \frac{2\rho e_b}{36} [3.0 + 4.5(\mathbf{e}_6 \cdot \mathbf{u}_b)^2 - 1.5(\mathbf{u}_b \cdot \mathbf{u}_b)] \\
&+ t_6 \dot{Q} \delta t + \mathbf{e}_6^2 (\bar{f}_6 + \bar{f}_8) \\
&- \mathbf{e}_6^2 (2t_6 \rho [1 + 4.5(\mathbf{e}_6 \cdot \mathbf{u}_b)^2 - 1.5(\mathbf{u}_b \cdot \mathbf{u}_b)]) , \\
\bar{g}_8 - \bar{g}_8^+ &= [\bar{g}_8 - \bar{g}_6] = 0,
\end{aligned}$$

$$\begin{aligned}
\text{if } \mathbf{e}_7 \cdot \mathbf{n} < 0 \quad (\Leftrightarrow \mathbf{e}_5 \cdot \mathbf{n} > 0); \quad \bar{g}_7 - \bar{g}_7^+ &= [\bar{g}_7 + \bar{g}_5] \\
&- \frac{2\rho e_b}{36} [3.0 + 4.5(\mathbf{e}_7 \cdot \mathbf{u}_b)^2 - 1.5(\mathbf{u}_b \cdot \mathbf{u}_b)] \\
&+ t_7 \dot{Q} \delta t + \mathbf{e}_7^2 (\bar{f}_7 + \bar{f}_5) \\
&- \mathbf{e}_7^2 (2t_7 \rho [1 + 4.5(\mathbf{e}_7 \cdot \mathbf{u}_b)^2 - 1.5(\mathbf{u}_b \cdot \mathbf{u}_b)]) , \\
\bar{g}_5 - \bar{g}_5^+ &= [\bar{g}_5 - \bar{g}_7] = 0,
\end{aligned}$$

$$\begin{aligned}
\text{if } \mathbf{e}_8 \cdot \mathbf{n} < 0 \quad (\Leftrightarrow \mathbf{e}_6 \cdot \mathbf{n} > 0); \quad \bar{g}_8 - \bar{g}_8^+ &= [\bar{g}_8 + \bar{g}_6] \\
&- \frac{2\rho e_b}{36} [3.0 + 4.5(\mathbf{e}_8 \cdot \mathbf{u}_b)^2 - 1.5(\mathbf{u}_b \cdot \mathbf{u}_b)] \\
&+ t_8 \dot{Q} \delta t + \mathbf{e}_8^2 (\bar{f}_8 + \bar{f}_6) \\
&- \mathbf{e}_8^2 (2t_8 \rho [1 + 4.5(\mathbf{e}_8 \cdot \mathbf{u}_b)^2 - 1.5(\mathbf{u}_b \cdot \mathbf{u}_b)]) , \\
\bar{g}_6 - \bar{g}_6^+ &= [\bar{g}_6 - \bar{g}_8] = 0.
\end{aligned}$$

Acknowledgments

This work is supported in part by the U.S. Department of Energy, Office of Nuclear Energy's Nuclear Energy University Programs, and in part by the U.S. Department of Energy, under Contract DE-ACO2-O6CH11357.

References

- [1] Merzari, E., Pointer, W. D., Smith, J. G., Tentner, A., & Fischer, P. (2012). Numerical simulation of the flow in wire-wrapped pin bundles: Effect of pin-wire contact modeling. *Nuclear Engineering and Design*, 253, 374-386.
- [2] Karniadakis, G. E. (1988). Numerical simulation of forced convection heat transfer from a cylinder in crossflow. *International Journal of Heat and Mass Transfer*, 31(1), 107-118.
- [3] Lange, C. F., Durst, F., & Breuer, M. (1998). Momentum and heat transfer from cylinders in laminar crossflow at $10^4 \leq Re \leq 200$. *International Journal of Heat and Mass Transfer*, 41(22), 3409-3430.
- [4] Wang, J., Wang, M., & Li, Z. (2007). A lattice Boltzmann algorithm for fluid-solid conjugate heat transfer. *International Journal of Thermal Sciences*, 46(3), 228-234.
- [5] Jain, P. C., & Goel, B. S. (1976). A numerical study of unsteady laminar

- forced convection from a circular cylinder. *Journal of Heat Transfer*, 98(2), 303-307.
- [6] Juncu, G. (2004). Unsteady conjugate heat/mass transfer from a circular cylinder in laminar crossflow at low Reynolds numbers. *International journal of heat and mass transfer*, 47(10), 2469-2480.
- [7] Das, M. K., & Reddy, K. (2006). Conjugate natural convection heat transfer in an inclined square cavity containing a conducting block. *International journal of heat and mass transfer*, 49(25), 4987-5000.
- [8] Jeon, B. J., Kim, Y. S., & Choi, H. G. (2012). Effect of the Reynolds number on the conjugate heat transfer around a circular cylinder with heat source. *Journal of mechanical science and technology*, 26(12), 3849-3855.
- [9] Chen, S., Doolen, G. D. (1998). Lattice Boltzmann method for fluid flows. *Annual review of fluid mechanics*, 30(1), 329-364.
- [10] Patel, S. S., Min, M., Uga, K. C., Lee, T. (2014). A spectral-element discontinuous Galerkin lattice Boltzmann method for simulating natural convection heat transfer in a horizontal concentric annulus. *Computers & Fluids*, 95, 197-209.
- [11] Jami, M., Mezrhab, A., & Lallemand, P. (2007). Lattice Boltzmann method applied to the laminar natural convection in an enclosure with

- a heat-generating cylinder conducting body. *International Journal of Thermal Sciences*, 46(1), 38-47.
- [12] Yan, Y. Y., & Zu, Y. Q. (2008). Numerical simulation of heat transfer and fluid flow past a rotating isothermal cylinder A LBM approach. *International Journal of Heat and Mass Transfer*, 51(9), 2519-2536.
 - [13] M. Min, T. Lee, A spectral-element discontinuous Galerkin lattice Boltzmann method for nearly incompressible flows, *J. Comput. Phys.* **230** 1 (2011) 245-259.
 - [14] X. Shan, H. Chen, Lattice Boltzmann model for simulating flows with multiple phases and components, *Phys. Rev. E* **47** 3 (1993) 1815-1819.
 - [15] X. He, S. Chen, G.D. Doolen, A novel thermal model for the lattice Boltzmann method in incompressible limit, *J. Comput. Phys.* **146** 1 (1998) 282-300.
 - [16] P. Fischer, J. Lottes, D. Pointer, A. Siegel, Petascale algorithms for reactor hydrodynamics, *Journal of Physics: Conference Series* **125** 1 (2008) 012076.
 - [17] Bhatnagar, P. L., Gross, E. P., & Krook, M. (1954). A model for collision processes in gases. I. Small amplitude processes in charged and neutral one-component systems. *Physical review*, 94(3), 511.
 - [18] Y.H. Qian, D. D’Humières, P. Lallemand, Lattice BGK models for Navier-Stokes equation, *Europhys. Lett.* **17** (1992) 479-484.

- [19] He, X., Shan, X., Doolen, G. D. (1998). Discrete Boltzmann equation model for nonideal gases. *Physical Review E*, 57(1), R13.
- [20] T. Lee, C.-L. Lin, An Eulerian description of the streaming process in the lattice Boltzmann equation, *J. Comput. Phys.* **185** 2 (2003) 445-471.
- [21] F.J. Alexander, S. Chen, J.D. Sterling, Lattice Boltzmann thermohydrodynamics, *Phys. Rev. E* **47** 4 (1993) R2249.
- [22] Z. Guo, C. Zheng, B. Shi, T.S. Zhao, Thermal lattice Boltzmann equation for low Mach number flows: Decoupling model, *Phys. Rev. E* **75** (2007) 036704.
- [23] Y. Peng, C. Shu, Y.T. Chew, Simplified thermal lattice Boltzmann model for incompressible thermal flows, *Phys. Rev. E* **68** (2003) 026701.
- [24] J.S. Hesthaven and T. Warburton, Nodal discontinuous Galerkin methods, algorithms, analysis, and applications, *Texts in Applied Mathematics* (Springer, 2008).
- [25] Q. Zou, X. He, On pressure and velocity boundary conditions for the lattice Boltzmann BGK model, *Phys. Fluids* **9** 6 (1997) 1591-1598.
- [26] M.O. Deville, P.F. Fischer, E.H. Mund, High-order methods for incompressible fluid flow, *Cambridge Monographs on Applied and Computational Mathematics* (Cambridge University Press, 2002).

The following paragraph should be deleted before the paper is published:
The submitted manuscript has been created by UChicago Argonne, LLC, Operator of Argonne National Laboratory (“Argonne”). Argonne, a U.S. Department of Energy Office of Science laboratory, is operated under Contract No. DE-AC02-06CH11357. The U.S. Government retains for itself, and others acting on its behalf, a paid-up nonexclusive, irrevocable worldwide license in said article to reproduce, prepare derivative works, distribute copies to the public, and perform publicly and display publicly, by or on behalf of the Government.